Dynamic surface reconstruction of individual gold nanoclusters by using a co-reactant enables color-tunable electrochemiluminescence

Yan-Mei Lei,[a,b] Di Wu,[c] Mei-Chen Pan,[a] Xiu-Li Tao,[a] Wei-Jia Zeng,[a] Li-Yong Gan,[c] Ya-Qin Chai,[a] Ruo Yuan,[a] and Ying Zhuo[a]*

[a] Key Laboratory of Luminescence Analysis and Molecular Sensing (Southwest University), Ministry of Education, College of Chemistry and Chemical Engineering, Southwest University, Chongqing 400715, China
E-mail: yingzhuo@swu.edu.cn (Y. Zhuo).

[b] Institute of Molecular Medicine, Renji Hospital, School of Medicine, Shanghai Jiao Tong University, Shanghai, 200127, China.

[c] College of Physics and Center of Quantum Materials and Devices, Chongqing University, Chongqing 401331, China

Table of Contents

1 Experimental Procedure

1.1 Materials

Glutathione (SG), gold chloride tetrahydrate ($HAuCl_4 \bullet 4H_2O$, 99.9%), cysteine, and tetra-n-butylammonium hexafluorophosphate ($TBAPF_6$) were received from Sigma Chemical Co. (St. Louis, MO, USA). Chitosan (CS) and pyridoxal 5-phosphate monohydrate (P5P) were purchased from Sangon Bioengineering Ltd. Acetic acid (99.7%), triethylamine (TEA), tri-n-propylamine (TPrA), sodium hydroxide (NaOH), sodium sulfide nonahydrate ($Na_2S \bullet 9H_2O$), and glutaraldehyde (50%) were purchased from Chengdu Chemical Reagent Company (Chengdu, China). Phosphate buffered saline (PBS, pH 7.4) solution was prepared using 0.1 M Na_2HPO_4, 0.1 M KH_2PO_4, and 0.1 M KCl. Ultrapure water was obtained by a Millipore Milli-Q water purification system with an electric resistance of 18.2 MΩ cm^{-1} and used throughout the experiment.

1.2 Apparatus

The measurements of cyclic voltammetry (CV) and electrochemiluminescence (ECL) were recorded on the MPI-E multifunctional electrochemical and chemiluminescent analytical system (Xi'an Remax Electronic Science &Technology Co. Ltd., Xi'an, China). The PMT was set at 600 V. Three-electrode systems consisted of an Ag/AgCl (saturated KCl) as a reference electrode, a platinum wire as the auxiliary electrode, and a glassy carbon electrode (GCE) as the working electrode, respectively. Fluorescence spectra were obtained with an RF-5301PC spectrophotometer (Shimadzu, Tokyo, Japan), and the UV-Vis spectrum was carried out with a UV-2450 spectrophotometer (Shimadzu, Tokyo, Japan). The ECL emission spectrum was obtained on a CHI 760E combined with a Newton EMCCD spectroscopy detector (Andor Co., Tokyo, Japan). The morphologies and sizes of the prepared nanomaterials were characterized by using a scanning electron microscope (SEM, S-4800, Hitachi, Tokyo, Japan) at an acceleration voltage of 20-30 kV and a high-resolution transmission electron microscope (HR-TEM, H600, Hitachi, Japan) at an acceleration voltage of 200 kV. X-ray photoelectron spectroscopy (XPS) measurements were collected on a VG Scientific ESCALAB 250 spectrometer (Thermoelectricity Instruments, USA). Steady-state luminescence lifetime measurements were recorded with an Edinburgh FLS 980 Lifetime and Steady State Spectrometer. Matrix-assisted laser desorption/ionization time-of-flight (MALDI-TOF) mass spectrometry was carried out on a Bruker Daltonics Autoflex II MALDI TOF/TOF system.

1.3 Synthesis of hierarchically porous hydrogel

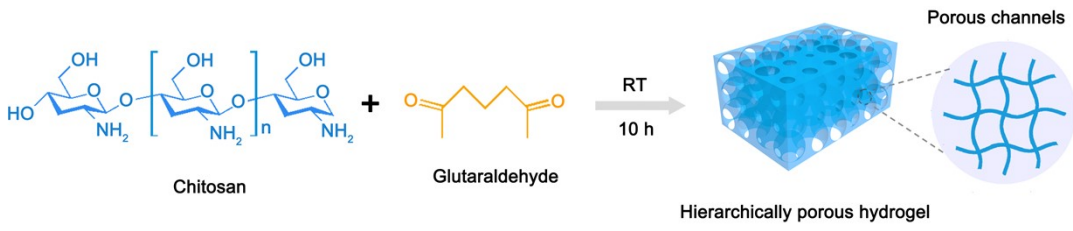

Scheme S1. Workflow for fabricating a hierarchically porous hydrogel.

The hierarchically porous hydrogel was synthesized as shown in Scheme S1. Concretely, the 4.0 mL chitosan (5.0 mg mL^{-1}) solution was prepared by mixing it with 0.5 vol.% aqueous acetic acid and ultrasonicating it continuously for 1 h. [1] Thereafter, 2 mL of glutaraldehyde solution was added to the above solution and mixed for 10 h at RT. Finally, the resultant hydrogel was washed in ultrapure water before being collected by centrifugation (10 000 rpm, 15 min) and redispersed in 20.0 mL of ultrapure water for further use.

1.4 Synthesis of hydrogel-confined Au NCs and discrete Au NCs

The hydrogel-confined Au NCs were prepared using the previous report with some modifications. [2] The hierarchically porous hydrogel with high water content could provide space for entrapping the reaction reagent. First, 2.5 mL of glutathione (SG, 0.1 M) was added to the above 4.0 mL hydrogel solution under constant ultrasonication for 30 min. The resultant hydrogel matrix is modified by SG, which can act as a ligand and a reducing reagent in generating Au NCs under alkaline conditions. Then, 0.5 mL of $HAuCl_4$ solution (1% wt) was mixed with the above solution under constant ultrasonication for 5 min. Thereafter, the pH of the mixture was adjusted to 11.0 with 1 M NaOH before being placed in an oven at 37 °C overnight to allow the Au NCs to localize within the hydrogel network. Finally, the resultant hydrogel-confined Au NCs product was collected by centrifugation (10 000 rpm, 15 min) and redispersed in 8.0 mL ultrapure water for further use.

The synthesis of discrete Au NCs protected without hydrogel was carried out under similar conditions described above.

1.5 ECL quantum yield of the hydrogel-confined Au NCs

The ECL quantum yield (Φ_{ECL}) was described as the ratio of the number of emission photons to that of chemiluminescent reactions between the redox species. The $[Ru(bpy)_3]^{2+}$ was used as a reference system to calculate Φ_{ECL} of the tested ECL emitters according to the relation below [3]:

$$\Phi_{ECL} = \Phi^{o}_{ECL} (I\, Q^{o}_{f} / I^{o}\, Q_{f})$$

Herein, Φ^{o}_{ECL} (5.0%) was the ECL quantum yield of 1 mM $[Ru(bpy)_3]^{2+}$ in 0.1 M $(TBA)BF_4$/ACN) through annihilation reaction, and the potential was cycled between 0 V and 1.5 V with a scan rate of 0.3 V s^{-1} [3-5]. Q_f and Q^{o}_{f} were the corresponding faradaic charges passed for the tested ECL emitters and $[Ru(bpy)_3]^{2+}$, respectively. I and I_o were the ECL intensities for the tested ECL emitters and $[Ru(bpy)_3]^{2+}$, respectively. For the detection of I and Q_f of the co-reactant ECL of hydrogel-confined Au NCs, 5.0 µL of hydrogel-confined Au NCs solution was carefully dropped onto the GCE surface and dried at RT before being detected in a 3.0 mL PBS (0.1 M, pH 7.4) solution containing 0.14 M TEA. For the detection of I and Q_f of the co-reactant ECL of discrete Au NCs, 5.0 µL of discrete Au NCs was dispersed in a 3.0 mL PBS (0.1 M, pH 7.4) solution containing 0.14 M TEA. These analyses were carried out using a scanning voltage of 0 V to 1.5 V and a scan rate of 0.3 V s^{-1}. For the detection of I and Q_f of the annihilation ECL of hydrogel-confined Au NCs, the potential was cycled between -2.0 V and 2.0 V with a scan rate of 0.3 V s^{-1} in 0.1 M $TBAPF_6$ acetonitrile solution.

1.6 Cells and culture conditions

The liver cancer cells (SMMC-7721) were grown in Dulbecco's modified Eagle's medium (DMEM) under oxidative stress conditions supplemented with fetal bovine serum (10%) and then maintained in a humidified atmosphere of 5% CO_2 at 37 °C. The cancer cells were grown to 90% confluence before cell inheritance. Considering their stable state, the third-generation cells were used for experiments. Cancer cells were collected and suspended in a cell culture medium at a concentration of 1.16×10^5 cells mL^{-1}.

1.7 µmapECL platform for sulfide detection

The quantitative analysis was performed by adding $Na_2S{\bullet}9H_2O$ as a source of sulfide. Initially, the GCE was polished with Al_2O_3 powder before being sonicated with ultrapure water and ethanol three times. Subsequently, 5.0 µL of hydrogel-confined Au NCs solution was carefully dropped onto the GCE surface and dried at RT. After that, different concentrations of Na_2S solution were added to a 0.1 M PBS (pH 7.4) solution containing 50 mM TEA. These analyses were carried out using a scan voltage of 0 to 1.5 V and a scan rate of 0.2 V s^{-1}.

1.8 ECL investigation of H_2S released from liver cancer cell

For ECL in situ detection of H_2S released from cancer cells, 10 µL of cell suspension (11.6 cells), 5 µL of 10 mM L-Cys, and 5 µL of 2 mM P5P were first dripped on the µmapECL platform, followed by incubation at 37 °C for 2 h. Finally, the H_2S was produced and directly detected in 3 mL of PBS

solution with 18 mM TEA as a co-reactant. For comparative analysis, the μmapECL platform was measured without stimulation under the same test condition.

In a 0.1 M PBS solution (pH 7.4), the distribution fraction (δ) of HS^- constituted about 80%, H_2S about 20%, and S^{2-} less than 1%. [6] Thus, when cells release H_2S in a PBS solution (pH 7.4), it mainly occurs in the following two forms: HS^- and H_2S.

1.9 Calculation details

Density functional theory (DFT) calculations have been performed using the Vienna Ab-initio Simulation Package [7, 8]. The interactions between ions and valence electrons were described by the projected augmented wave method, and the exchange-correlation energy was treated by using the Perdew-Burke-Ernzerhof functional based on the generalized gradient approximation [9, 10]. The kinetic energy cut-off of the plane wave basis set was set to 500 eV, and a gamma-centered 1×1×1 k-point mesh was used for the calculations. The D3 method with Becke-Jonson damping was considered to correct the dispersion interactions [11]. All atoms were fully relaxed until the total energy and the force declined below 10^{-5} eV and 0.02 eV $Å^{-1}$, respectively. Spin polarization was considered in all calculations. The thiolated gold nanoclusters ($Au_{15}(SCH_3)_{13}$) were modeled in a big lattice, including 15 Au atoms, 13 S atoms, 13 C atoms, and 39 H atoms. A large vacuum space was used along the a, b, and c directions to avoid periodic interactions.

2. Supplementary Results

2.1 Zeta potentials of hydrogel and SG-functionalized hydrogel

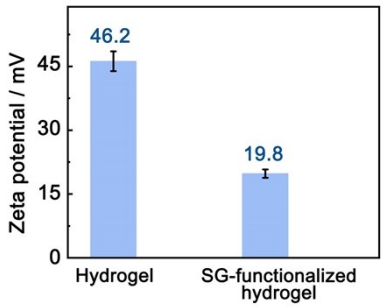

Fig. S1 Zeta potentials of hydrogel and SG-functionalized hydrogel.

2.2 HR-TEM images and SAED pattern of hydrogel-confined Au NCs.

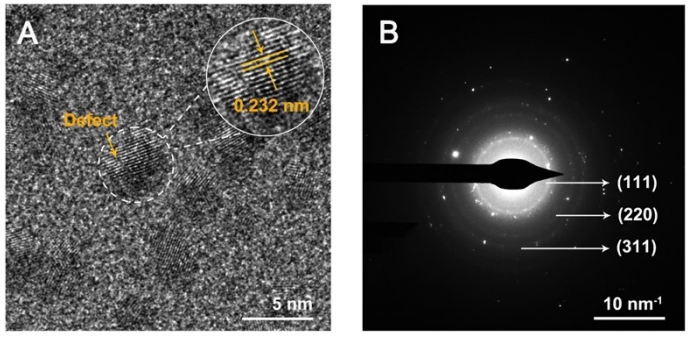

Fig. S2 High-resolution transmission electron microscopy (HR-TEM) images (A) and elected area electron diffraction pattern (SAED) pattern (B) of hydrogel-confined Au NCs. Inset A crystalline structure of Au NCs within the hydrogel matrix.

2.3 Energy-dispersive X-ray element analysis of hydrogel-confined Au NCs

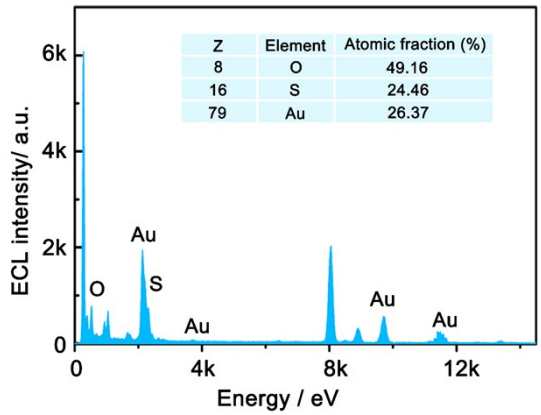

Fig. S3 Energy-dispersive X-ray element analysis of hydrogel-confined Au NCs.

2.4 MALDI-TOF mass spectrum of the discrete Au NCs

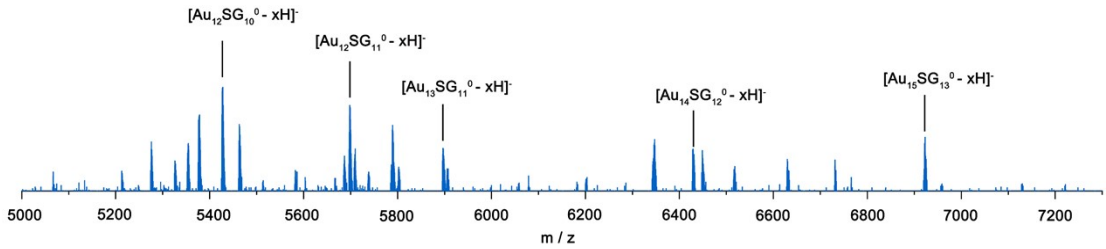

Fig. S4 Negative linear mode MALDI-TOF mass spectrum of the discrete Au NCs using DCTB matrix.

The chemical composition of the discrete Au NCs was analyzed using matrix-assisted laser desorption ionization time-of-flight mass spectroscopy (MALDI-TOF MS). The spectrum was collected in negative-ion mode using the DCTB matrix. As shown in Fig. S4, the first peak at m/z 5427 could be assigned to $[Au_{12}SG_{10}^{0} - xH]^-$; the second peak at m/z 5698 could be assigned to the fragment peak of $[Au_{12}SG_{11}^{0} - xH]^-$; the third peak at m/z 5896 could be assigned to the fragment peak of $[Au_{13}SG_{11}^{0} - xH]^-$; the fourth peak at m/z 6429 could be assigned to the fragment peak of $[Au_{14}SG_{12}^{0} - xH]^-$; the fifth peak at m/z 6923 could be assigned to the fragment peak of $[Au_{15}SG_{13}^{0} - xH$. Thus, the precise chemical composition of discrete Au NCs was determined to be $Au_{12\text{-}15}SG_{12\text{-}13}$ species.

Because chitosan is a macromolecule with a very large molecular weight, we cannot determine the molecular structure of hydrogel-confined Au NCs by mass spectrometry. The essentially identical absorption profiles for hydrogel-confined Au NCs, discrete Au NCs, and the mixture of Au NCs and hydrogel (Fig. 4A-C) confirm that the size of the Au cores is unaffected by hydrogel matrix, [12, 13] and that these nanoclusters have the same number of atoms, corresponding to the ground-state absorption energy of $Au_{12\text{-}15}SG_{12\text{-}13}$ species.[2, 14] Therefore, we confirm the precise structure of the discrete Au NCs by mass spectrometry measurement, and the hydrogel-confined Au NCs and discrete Au NCs were determined to be $Au_{12\text{-}15}SG_{12\text{-}13}$ species.

2.5 ECL-voltage and CV curves of hydrogel-confined Au NCs in PBS solution

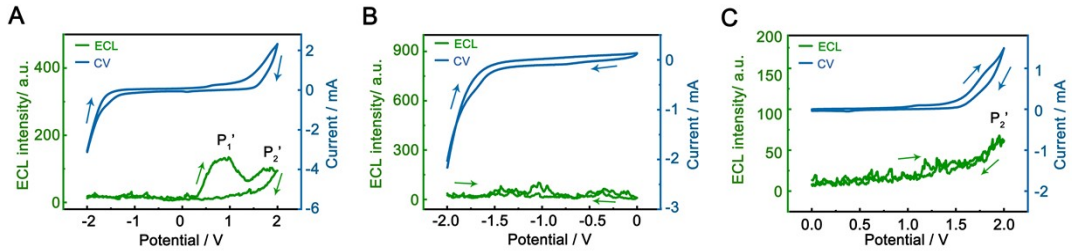

Fig. S5 ECL-voltage (green line) and CV (blue line) curves of hydrogel-confined Au NCs recorded during potential scanning (A) between -2.0 V and 2.0 V, (B) between -2.0 V and 0 V, and (C) between 0 V and 2.0 V in 0.1 M PBS solution.

To investigate the effect of hydrogel on the ECL of Au NCs, the ECL and cyclic voltammogram (CV) curves were recorded during different potential scanning in 0.1 M PBS solution without TEA reagent. As shown in Fig. S5A, two weak ECL peaks (P_1' and P_2') are observed during potential scanning between -2.0 V and 2.0 V. However, almost no ECL signal is observed during potential scanning between -2.0 V and 0 V (Fig. S5B); only an extremely weak ECL peak of P2' is observed during potential scanning between 0 V and 2.0 V (Fig. S5C). These comparison results demonstrated that hydrogel is mainly used as a supporter rather than a co-reactant like TEA.

2.6 Influence of storage time on the ECL intensity and wavelength of hydrogel-confined Au NCs and discrete Au NCs

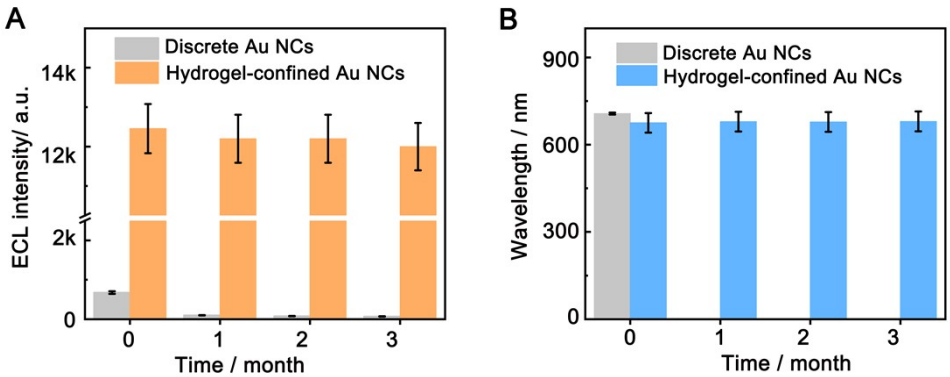

Fig. S6 The influence of storage time on the (A) ECL intensity and (B) wavelength of hydrogel-confined Au NCs and discrete Au NCs. The experiments were carried out with a voltage scan ranging from 0 to 1.5 V in 0.1 M PBS (pH 7.4) solution containing 18 mM TEA as a co-reactant.

A series of experiments were done, as shown in Fig. S6A and 6B, to investigate the potential influence of storage time on the ECL intensity and wavelength of hydrogel-confined Au NCs and discrete Au NCs. The hydrogel-confined Au NCs stored at 4 °C for 3 months without obvious ECL intensity and wavelength changes. When the storage time of discrete Au NCs exceeds one month, there is a notable decrease in their ECL intensity, rendering the analysis of their ECL wavelength unachievable.

2.7 ECL stability of the hydrogel-confined Au NCs

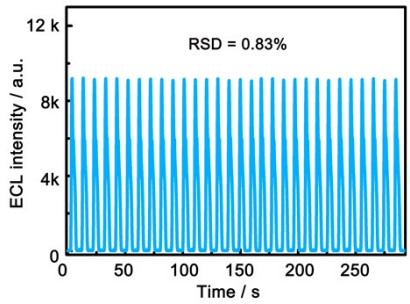

Fig. S7 ECL stability of the hydrogel-confined Au NCs under consecutive cyclic scan of 30 cycles. The experiment was carried out by scanning the potential from 0 to 1.5 V in 0.1 M PBS (pH 7.4) solution with 100 mM TEA as a co-reactant.

2.8 ECL repeatability of the hydrogel-confined Au NCs

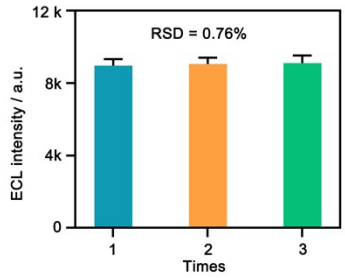

Fig. S8 ECL repeatability of the hydrogel-confined Au NCs by 3 parallel measurements. The experiment was carried out by scanning the potential from 0 to 1.5 V in 0.1 M PBS (pH 7.4) solution with 100 mM TEA as a co-reactant.

2.9 ECL transients of hydrogel-confined Au NCs/TEA system by different pulse potentials

To determine the appropriate conditions for ECL generation, as shown in Fig. S9 the oxidative process-initiated ECL of hydrogel-confined Au NCs was investigated in PBS solution with TEA as a co-reactant by different pulse potentials. An extremely weak ECL signal was observed by stepping from 0 V to 0.7 V, where the TEA could be sufficiently oxidized to the highly reducing agent ($TEA^{\bullet}$) and the Au NCs already underwent an oxidation reaction for Au NCs^0 to Au NCs+, indicating that the generated Au NCs^+ was not the rate-determining step for ECL generation. The ECL intensity was increased dramatically upon stepping at more positive potentials from 0 to 0.9 V, 1.1, 1.3, and 1.5 V, which proved that three electrochemical hole-injection processes for Au NCs to Au NCs^{2+}, Au NCs^{3+}, and Au NCs^{4+}, respectively, were the rate-determining steps for ECL generation. However, the decrease in ECL intensity was observed at a more positive potential from 0 to 1.7 V, which proved that the chemical stability of the oxidized Au NCs was interfered with by the high over-potential.

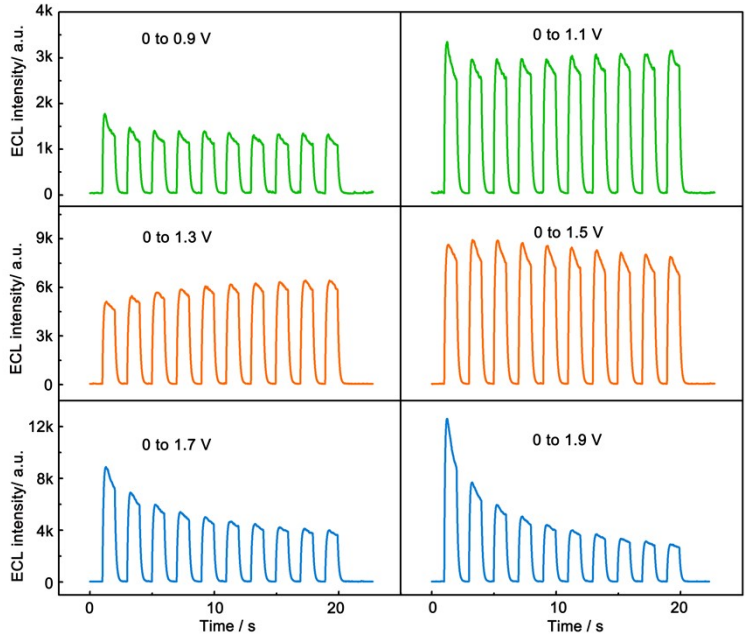

Fig. S9 ECL signals of hydrogel-confined Au NCs in 0.1 M PBS (pH 7.4) solution containing 18 mM TEA as a co-reactant by different pulse potentials from 0 V to 0.9 V, 1.1 V, 1.3 V, 1.5 V, 1.7V, and 1.9 V, respectively. Each pulse potential was held for 1 s.

2.10 Spooling ECL spectra of hydrogel-confined Au NCs recorded in the annihilation path

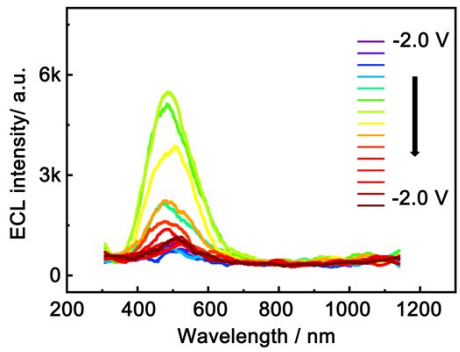

Fig. S10 Spooling ECL spectra of hydrogel-confined Au NCs recorded in 0.1 M $TBAPF_6$ acetonitrile solution. The applied potential is swept between -2.0 V and 2.0 V.

2.11 Influence of scan rate, scan voltage, and pH on ECL wavelength of hydrogel-confined Au NCs/TEA system

To investigate the influence of scan rate, scan voltage, and pH on the ECL wavelength of a hydrogel-confined Au NCs/triethylamine (TEA) system, the ECL spectra were measured by adjusting these parameters in a 0.1 M phosphate-buffered saline (PBS, pH 7.4) solution with a TEA concentration of 125 mM as a co-reactant.

Fig. S11A shows the influence of the scan rate on both the ECL intensity and wavelength of the hydrogel-confined Au NCs/TEA system. The intensity and wavelength of core-related ECL remain almost unchanged. However, the maximum intensity and wavelength of surface-related ECL were obtained at a scan rate of 0.2 V s^{-1} as the scan rate changed from 0.1 to 0.5 V s^{-1}. The wavelength of surface-related ECL exhibits a color-tunable range of 788-821 nm, while the wavelength of core-related ECL remained constant at 489 nm. The following factors may contribute to this ECL

phenomenon: (1) When the scan rate is slow, the amount of TEA radicals per unit time is small as a result of decomposition that is enhanced on these longer timescales.[15] (2) Due to the excessively rapid scan rate, the electrochemical hole-injection processes for TEA-to-TEA radicals were the rate-determining step for ECL intensity and wavelength.[16]

The scan voltage effect on the ECL intensity and wavelength of the hydrogel-confined Au NCs/TEA system is shown in Fig. S11B. The intensity and wavelength of core-related ECL remain almost unchanged. However, the maximum intensity and wavelength of surface-related ECL were obtained at a scan voltage of 1.5 V as the scan voltage changed from 1.0 to 2.0 V. The wavelength of surface-related ECL exhibits a color-tunable range of 802-823 nm, while the wavelength of core-related ECL remained constant at 489 nm. The following factors may contribute to this ECL phenomenon: (1) When the scan voltage was low, the amount of TEA radicals produced by slow electrode oxidation was the primary determinant of ECL intensity and wavelength. [17] (2) Because the scan voltage was too high, the stability of the TEA radicals was interfered with by side reactions (i.e., dissolved oxygen) in an aqueous solution.[18]

The pH effect on the ECL intensity of the hydrogel-confined Au NCs/TEA system is shown in Fig. S11C. The intensity and wavelength of core-related ECL remain almost unchanged. However, the maximum ECL intensity and wavelength were obtained at pH 8.5 as the pH values changed from 4.5 to 12.5. The surface-related ECL wavelength was shifted from 625 to 829 nm, while the ECL peak of core-related ECL remained constant at 489 nm. The following factors may contribute to this ECL phenomenon: (1) When the pH of the solution was too low, the TEA was easily converted to protonated $TEAH^+$ at the working potential, perhaps impeding TEA reduction.[17] (2) Because the pH of the solution was too high, the cation products were consumed by the scavenging reaction with hydroxide ions. [19]

Collectively, the ECL process of the hydrogel-confined Au NCs/TEA system is photon generation by hole-injection injection, and its intensity and wavelength in general depend on the availability and stability of the TEA radicals. The surface-related ECL wavelength of hydrogel-confined Au NCs was easily modulated by adjusting the pH, scan rate, and scan voltage with TEA as a co-reactant. This further demonstrates that TEA radicals can interact with the Au shell and easily affect the surface-related rather than the core-related ECL wavelength.

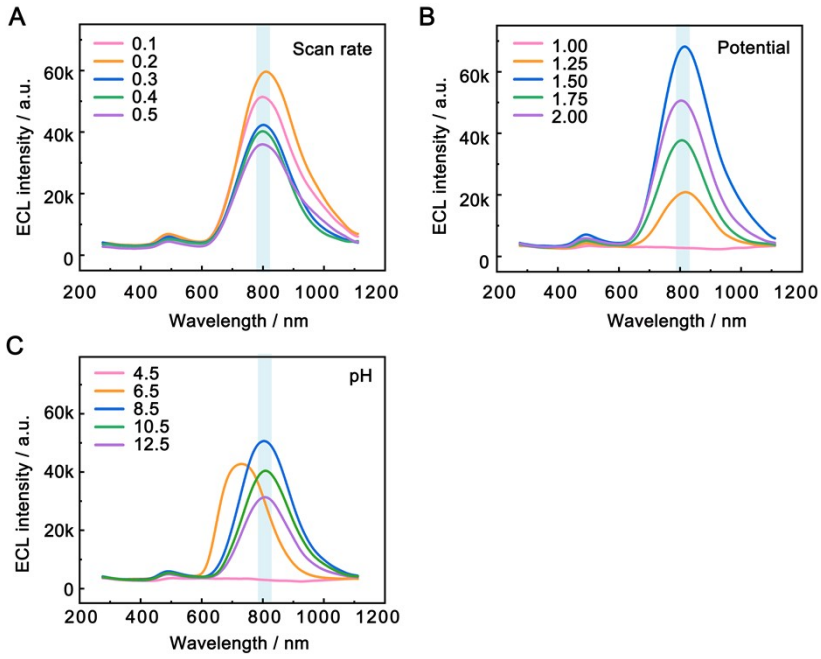

Fig. S11 ECL spectra of hydrogel-confined Au NCs recorded in 0.1 M PBS (pH 7.4) solution with 125 mM TEA as co-reactant at (A) scan voltage of 0 to 1.5 V by varying scan rate (from 0.1 to 0.5 V s^{-1}), (B) scan rate of 0.2 V s^{-1} by varying scan voltage (from 0.1 to 1.0, 1.25, 1.5, 1.75, and 2.0 V), and (C) scan rate of 0.2 V s^{-1} and scan voltage of 0 to 1.5 V by varying pH (4.5, 6.5, 8.5, 10.5, and 12.5).

2.12 Raman spectrum of hydrogel-confined Au NCs/TEA system

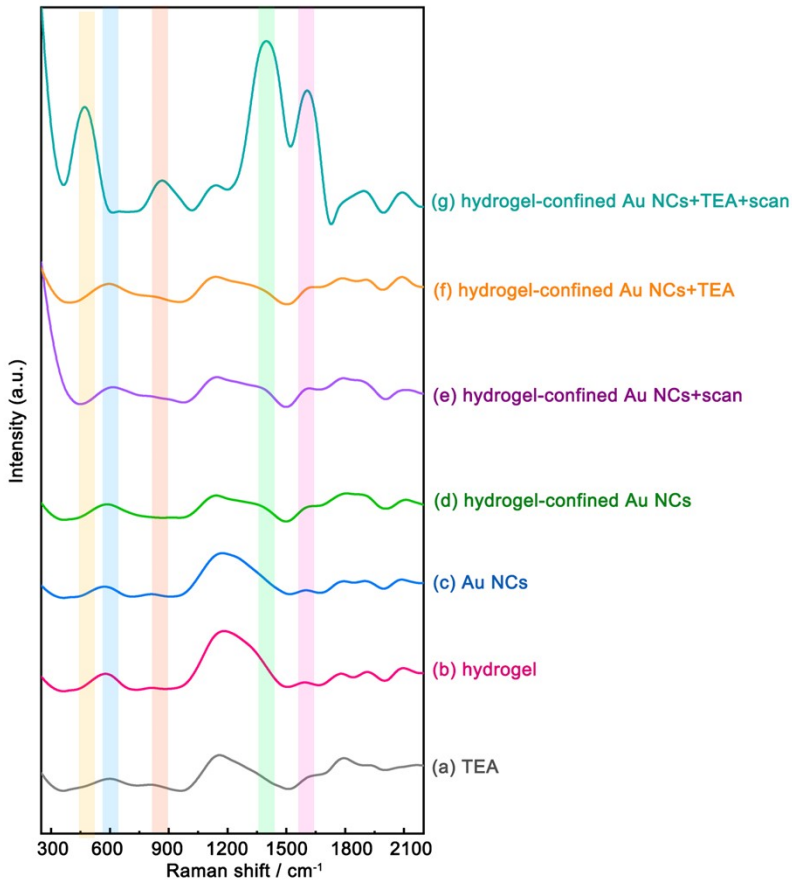

Fig. S12 Raman spectrum of (a) TEA, (b) hydrogel, (c) Au NCs, (d) hydrogel-confined Au NCs, (e) hydrogel-confined Au NCs + CV scan, (f) hydrogel-confined Au NCs +TEA, (g) hydrogel-confined Au NCs +TEA+ CV scan. Each CV scan was held for 50 s with scan potential from 0 to 1.5 V and a scan rate of 0.2 V s^{-1}.

Raman spectroscopy is a non-destructive and surface-sensitive technique, which enables the characterization of structural changes, identification of new species, and monitoring of surface reactions, providing a deeper understanding of the surface properties and reactivity of nanoclusters.[20-22] Surface reconstruction in nanoclusters often leads to changes in their vibrational properties, resulting in shifts in the Raman peaks. These shifts can be attributed to alterations in bond lengths, bond strengths, or the coordination environment of atoms at the surface. Thus, by monitoring the shifts in Raman peaks, researchers can identify and quantify the extent of surface reconstruction.

Fig. S12 displays a series of Raman experiments conducted to investigate the surface reconstruction of Au NCs. The Raman peaks of TEA, hydrogel, Au NCs, and hydrogel-confined Au NCs are almost identical (curves a-e): C-N stretching vibrations (550-600 cm^{-1}), N-C-H bending vibrations (600-900 cm^{-1}), C-O stretching vibrations (1050-1150 cm^{-1}), glycosidic linkage vibration (1080-1100 cm^{-1}), N-C-C stretching (1100-1300 cm^{-1}), C-N-H bending region (1290-1350 cm^{-1}), amide I band (1645-1660 cm^{-1}), amide II band, (1530-1560 cm^{-1}), and C=O stretching vibrations (1650-1750 cm^{-1}). [23, 24] The Raman peak of hydrogel-confined Au NCs remains unchanged after electrochemical scanning (curve f), but the Raman peak of the hydrogel-confined Au NCs/TEA system grows stronger and produces a new Raman peak (curve g). The hydrogel-confined Au NCs/TEA system exhibits the following characteristics upon electrochemical scanning: (1) two distinct Raman peaks are seen at around 1610 cm^{-1} and 1350 cm^{-1}, which may be induced by the particular vibration of alkylamine radicals; [25, 26] (2) a distinct Raman peak is discovered at approximately 474 cm^{-1}, matching to the gold-gold vibration mode. [27, 28] In general, the appearance of new Raman peaks can be attributed to the presence of amine radicals formed during the electrochemical reaction. Additionally, the

interaction between these TEA radicals and the surface of Au NCs can result in a localized amplification of the electric field, thereby augmenting their Raman signal.

Collectively, Raman spectroscopy demonstrated the specific peaks in the adsorption of TEA• caused by surface defects of Au NCs.

2.13 DFT calculation results for $Au_{15}(SR)_{13}$

Table S1. Atoms charges of bare Au NCs, Au NCs-1ad, and Au NCs-2ad.

Atoms	Atom charge / e (Au NCs)	Atom charge / e (Au NCs-1ad)	Atom charge / e (Au NCs-2ad)
1(Au1）	10.944768	10.94737	10.967374
2(Au2)	10.953777	10.968119	11.032491
3(Au3)	10.968239	10.965177	10.975552
4(Au4)	10.890374	10.88792	10.886592
5(Au5)	10.876107	10.886802	10.693314
6(Au6）	10.870975	10.872274	10.873387
7(Au7)	10.87432	10.858661	10.864357
8(Au8)	10.868363	10.871006	10.873182
9(Au9)	10.861654	10.865567	10.871622
10(Au10)	10.86145	10.854058	10.853768
11(Au11)	10.858404	10.857385	10.861605
12(Au12)	10.944564	10.943403	10.958839
13(Au13)	10.875733	10.883381	10.885189
14(Au14)	10.877373	10.768423	10.719309
15(Au15)	10.873991	10.878962	10.88743
16(S1)	6.174615	6.171121	6.141057
17(S2)	6.167294	6.17129	6.167355
18(S3)	6.164683	6.161521	6.161683
19(S4)	6.160227	6.144634	6.177051
20(S5)	6.16676	6.151649	6.144261
21(S6)	6.165397	6.1686	6.150525
22(S7)	6.147387	6.177036	6.170763
23(S8)	6.147299	6.15208	6.144868
24(S9)	6.163175	6.17159	6.166988
25(S10)	6.173291	6.180904	6.171138
26(S11)	6.18403	6.168798	6.172991
27(S12)	6.150055	6.149195	6.150929
28(S13)	6.16937	6.17296	6.188707

Table S2. Bond Lengths of bare Au NCs, Au NCs-1ad, and Au NCs-2ad.

Bond	Bond Length / Å (Au NCs)	Bond Length / Å (Au NCs-1ad)	Bond Length / Å (Au NCs-2ad)
Au1-S13	2.351	2.364	2.391
Au2-S11	2.344	2.34	2.472
Au3-S2	2.433	2.42	2.446
Au4-S2	2.314	2.311	2.298
Au4-S3	2.323	2.323	2.304
Au5-S3	2.325	2.324	2.384
Au5-S1	2.323	2.323	2.376
Au6-S1	2.321	2.32	2.302
Au6-S4	2.317	2.316	2.31
Au7-S5	2.317	2.321	2.316
Au7-S7	2.318	2.324	2.315
Au8-S7	2.32	2.319	2.318
Au8-S12	2.312	2.311	2.315
Au9-S6	2.385	2.387	2.392
Au9-S5	2.39	2.388	2.385
Au10-S12	2.332	2.332	2.327
Au10-S8	2.326	2.327	2.323
Au11-S8	2.322	2.321	2.316
Au11-S6	2.317	2.315	2.315
Au12-S4	2.339	2.335	2.366
Au13-S9	2.303	2.286	2.287
Au13-S10	2.319	2.337	2.34
Au14-S9	2.309	2.367	2.372
Au14-S11	2.3	2.34	2.344
Au15-S10	2.323	2.328	2.324
Au15-S13	2.311	2.308	2.319

2.14 Schematic of ECL mechanism of hydrogel-confined Au NCs

The schematic diagram illustrating the annihilation-type and co-reactant-type ECL mechanism of hydrogel-confined Au NCs is shown as follows:

The annihilation-type ECL reaction paths of the hydrogel-confined Au NCs are illustrated in Fig. S13A.[29] The production of both reduced and oxidized forms of Au NCs is facilitated by electron transfer processes occurring at the electrode, as outlined in Equation (1-2). The interaction between the two distinct radical intermediates, as shown by Equation 3, results in the emission of core-related light by the excited Au NCs* in Equation 4.

In contrast to previously documented Au NCs, the co-reactant-type ECL reaction paths of the hydrogel-confined Au NCs are associated with both the Au(0) core and the Au(I)-S surface (Fig. S13B). During the positive potential scanning, the Au NCs underwent oxidation to form Au $NCs^{+\bullet}$ as described by Equation 5. Meanwhile, the co-reactant TEA underwent electro-oxidation to form $TEA^{+\bullet}$ and subsequently underwent deprotonation to generate a $TEA^{\bullet}$ (Equation 6). The reduction of Au $NCs^{+\bullet}$ by $TEA^{\bullet}$ leads to the generation of excited Au NCs^{*} (Equation 7), resulting in the core-related ECL signal (Equation 8).[3] Strikingly, surface-related ECL emission is observed as a result of the surface reconstruction of Au $NCs^{+\bullet}$ and $TEA^{\bullet}$. This process leads to the generation of excited exciplexes [Au NCs, $TEA_{oxidate}$]* (Equation 9),[30] resulting in the surface-related ECL signal (Equation 10).

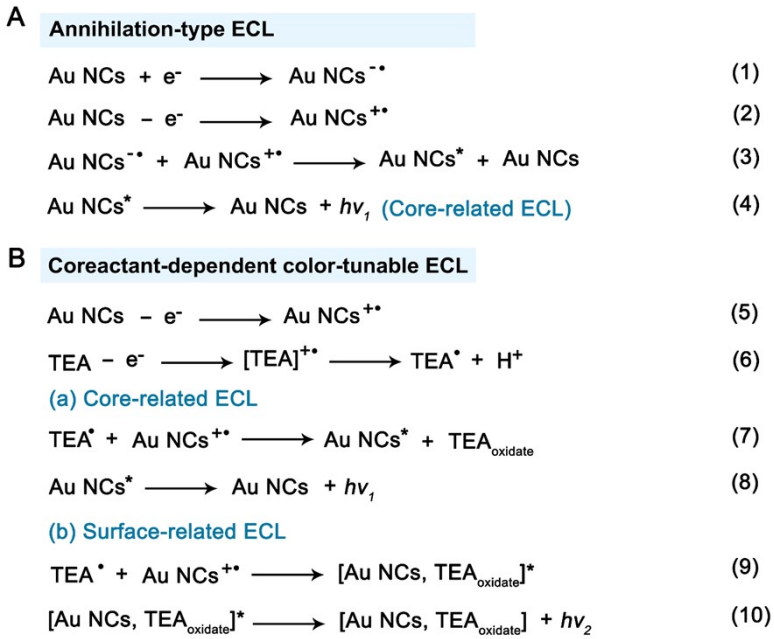

Fig. S13 Schematic of annihilation-type (A) and co-reactant-type (B) ECL pathways for hydrogel-confined Au NCs.

2.15 Microenvironment mapping on tumor cell-derived sulfides using µmapECL platform

The extracellular microenvironment is a complex, dynamic, and local environment in which cells can communicate by processing numerous biological events [31]. Understanding cellular physiological processes, particularly tumor cell metabolism and signal transduction, requires accurate monitoring of the fluctuating extracellular surroundings. Here we develop a microenvironment-mapping ECL (µmapECL) platform that utilizes hydrogel-confined Au NCs as the mapping matrix to selectively monitor the cell-microenvironment interactions. To evaluate the potential application of the µmapECL platform in tumor diagnosis, liver cancer cells (SMMC-7721) are selected as the model for endogenous hydrogen sulfide (H_2S) analysis (Fig. S14A), where H_2S is produced from cysteine or cysteine derivatives catalyzed by cystathionine α-synthase and cystathionine γ-lyase. The liver cancer cells first adhered to the surface of the µmapECL platform. Then, cysteine and pyridoxal 5-phosphate

monohydrate (P5P) are used to stimulate cancer cells to release more H_2S [32]. Finally, the H_2S is produced and directly detected by the μmapECL platform.

Before use, the sensitivity of the μmapECL platform is assessed by measuring the ratio of the change of ECL intensity (ΔI) and wavelength ($\Delta\lambda$) after incubation with Na_2S. As shown in Fig. S14B, the I declined and the λ blued gradually with the increase of Na_2S concentration from 1.0×10^{-13} to 1.0×10^{-7} M. The excellent linear relationship between the $\lg\Delta I/\lg\Delta\lambda$ and the logarithmic value of sulfide concentrations ($\lg c$) is shown in Fig. S14C. The regression equation is expressed as $\lg\Delta I/\lg\Delta\lambda = -0.113 \lg c + 1.32$, and the limit of detection (S/N = 3) is 3.2×10^{-14} M. In addition, the proposed platform is compared with fluorescence and electrochemical methods (Table S3), which exhibit high sensitivity for sulfide analysis. Then, the selectivity of the proposed platform is further evaluated by sulfides and several interfering ions (including SO_4^{2-}, SO_3^{2-}, HCO_3^-, NO_3^-, F^-, Br-, and NO_2^-). As shown in Fig. S14D, compared to the interfering ions (1.0×10^{-10} M), the $\Delta\lambda$ *or* ΔI of the proposed platform increased dramatically in the presence of Na_2S (1.0×10^{-12} M), which indicated that the proposed platform possessed excellent selectivity for H_2S detection. According to the calibration equation obtained and the stimulated ECL response (Fig. S14E), the H_2S concentration is calculated as 0.12 nM with an average cell count of 11.6. Therefore, this proposed method accurately represents monitoring tumor cell-derived H_2S under oxidative stress conditions.

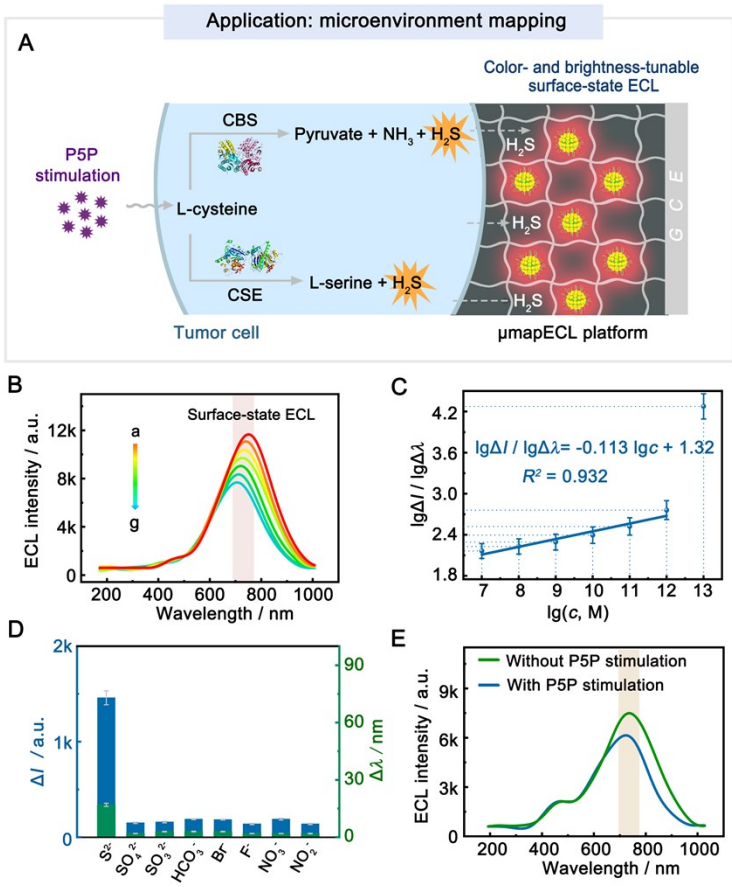

Fig. S14 (A) Schematic depicting the hydrogel-confined Au NCs as the mapping matrix to monitor the tumor cell-derived H_2S selectively on drug stimulation. (B) ECL response of the μmapECL platform toward different concentrations of Na_2S. (C) Calibration plot for the $\lg\Delta I/\lg\Delta\lambda$ vs. $\lg c$. (D) Selectivity of the μmapECL platform. (E) ECL responses of the tumor cell adhered on the surface of the μmapECL platform without (green line) and with (blue line) P5P stimulation.

2.16 Comparison of the different methods for sulfide detection

Table S3. Comparison of the different methods for sulfide detection.

Methods	Detection Limit	Dynamic Range	Ref
fluorescence	8.3×10^{-10} M	0 to 9×10^{-6} M	33
fluorescence	5.3×10^{-8} M	0 to 1.5×10^{-5} M	34
fluorescence	4.5×10^{-8} M	0 to 8.0×10^{-5} M	35
Absorption	5.9×10^{-7} M	0 to 1.0×10^{-4} M	36
electrochemical	4.0×10^{-11} M	1.0×10^{-10} to 5.0×10^{-7} M	37
ECL	----	5.0×10^{-9} to 2.0×10^{-5} M	38
ECL	3.2×10^{-14} M	1.0×10^{-12} to 1.0×10^{-7} M	This work

3. References

1. S. Takeshita, A. Konishi, Y. Takebayashi, S. Yoda and K. Otake, *Biomacromolecules*, 2017, **18**, 2172-2178.
2. Z. Luo, X. Yuan, Y. Yu, Q. Zhang, D. T. Leong, J. Y. Lee and J. Xie, *J. Am. Chem. Soc.*, 2012, **134**, 16662-16670.
3. H. Peng, Z. Huang, Y. Sheng, X. Zhang, H. Deng, W. Chen and J. Liu, *Angew. Chem. Int. Ed.*, 2019, **58**, 11691-11694.
4. F. Wang, J. Lin, T. Zhao, D. Hu, T. Wu and Y. Liu, *J. Am. Chem. Soc.*, 2016, **138**, 7718-7724.
5. H. Peng, Z. Huang, H. Deng, W. Wu, K. Huang, Z. Li, W. Chen and J. Liu, *Angew. Chem. Int. Ed.*, 2020, **59**, 9982-9985.
6. M. Asif, A. Aziz, Z. Wang, G. Ashraf, J. Wang, H. Luo, X. Chen, F. Xiao and H. Liu, *Anal. Chem.* , 2019, **91**, 3912-3920.
7. G. Kresse and J. Furthmüller, *Phys. Rev. B*, 1996, **54**, 11169-11186.
8. G. Kresse and J. Furthmüller, *Comp. Mater. Sci.* , 1996, **6**, 15-50.
9. C. Filippi, D. J. Singh and C. J. Umrigar, *Phys. Rev. B*, 1994, **50**, 14947.
10. J. P. Perdew, K. Burke and M. Ernzerhof, *Phys. Rev. Lett.*, 1996, **77**, 3865.
11. S. Grimme, J. Antony, S. Ehrlich and H. Krieg, *J. Chem. Phys.*, 2010, **132**, 154104.
12. B. Santiago-Gonzalez, A. Monguzzi, J. M. Azpiroz, M. Prato, S. Erratico, M. Campione, R. Lorenzi, J. Pedrini, C. Santambrogio, Y. Torrente, F. De Angelis, F. Meinardi and S. Brovelli, *Science*, 2016, **353**, 571-575.
13. B. Santiago-Gonzalez, A. Monguzzi, C. Capitani, M. Prato, C. Santambrogio, F. Meinardi and S. Brovelli, *Angew. Chem. Int. Ed.*, 2018, **57**, 7051-7055.
14. B. Santiago-Gonzalez, A. Monguzzi, J. M. Azpiroz, M. Prato, S. Erratico, M. Campione, R. Lorenzi, J. Pedrini, C. Santambrogio, Y. Torrente, F. De Angelis, F. Meinardi and S. Brovelli, *Science*, 2016, **353**, 571-575.
15. R. R. Maar, R. Z. Zhang, D. G. Stephens, Z. F. Ding and J. B. Gilroy, *Angew. Chem. Int. Ed.*, 2019, **58**, 1052-1056.
16. M. Hesari, K. N. Swanick, J. S. Lu, R. Whyte, S. Wang and Z. Ding, *J. Am. Chem. Soc.*, 2015, **137**, 11266-11269.
17. T. Y. Wang, D. C. Wang, J. W. Padelford, J. Jiang and G. L. Wang, *J. Am. Chem. Soc.*, 2016, **138**, 6380-6383.
18. W. J. Zeng, K. Wang, W. B. Liang, Y. Q. Chai, R. Yuan and Y. Zhuo, *Chem. Sci.*, 2020, **11**, 5410-5414.
19. C. M. Cheng, Y. Huang, X. Q. Tian, B. Z. Zheng, Y. Li, H. Y. Yuan, D. Xiao, S. P. Xie and M. M. F. Choi, *Anal. Chem.*, 2012, **84**, 4754-4759.
20. W. G. Su, J. Zhang, Z. C. Feng, T. Chen, P. L. Ying and C. Li, *J. Phys. Chem. C* 2008, **112**, 7710-7716.
21. A. Urakawa, N. Maeda and A. Baiker, *Angew. Chem. Int. Ed.*, 2008, **47**, 9256-9259.
22. H. Zhang, S. Duan, P. M. Radjenovic, Z. Q. Tian and J. F. Li, *Acc. Chem. Res.* , 2020, **53**, 729-739.
23. F. Usman, J. O. Dennis, K. C. Seong, A. Y. Ahmed, F. Meriaudeau, O. B. Ayodele, A. R. Tobi, A. A. S. Rabih and A. Yar, *Results Phys.*, 2019, **15**, 102690.

24. S. Gohda, M. Saito, Y. Yamada, S. Kanazawa, H. Ono and S. Sato, *J. Mater. Sci.*, 2021, **56**, 2944-2960.
25. O. Zabihi, M. Ahmadi, S. Shafei, S. M. Seraji, A. Oroumei and M. Naebe, *Compos. Part A Appl. Sci. Manuf.*, 2016, **88**, 243-252.
26. J. Chen, D. Unjaroen, S. Stepanovic, A. van Dam, M. Gruden and W. R. Browne, *Inorg. Chem.*, 2018, **57**, 4510-4515.
27. S. Govindaraju, M. Ramasamy, R. Baskaran, S. J. Ahn and K. Yun, *Int. J. Nanomed.* , 2015, **10**, 67-78.
28. S. D. Hanna, S. I. Khan and J. I. Zink, *Inorg. Chem.*, 1996, **35**, 5813-5819.
29. S. Chen, H. Ma, J. W. Padelford, W. Qinchen, W. Yu, S. Wang, M. Zhu and G. Wang, *J. Am. Chem. Soc.*, 2019, **141**, 9603-9609.
30. P. Zhang, Z. Xue, D. Luo, W. Yu, Z. Guo and T. Wang, *Anal. Chem.*, 2014, **86**, 5620-5623.
31. Z. Xiang, J. Zhao, J. Qu, J. Song and L. Li, *Angew. Chem. Int. Ed.*, 2022, **61**, e202111836.
32. J. Guo, L. Yang, H. Xu, C. Zhao, Z. Dai, Z. Gao and Y. Song, *Anal. Chem.* , 2019, **91**, 13746-13751.
33. W.-Y. Chen, G.-Y. Lan and H.-T. Chang, *Anal. Chem.* , 2011, **83**, 9450-9455.
34. F. Wang, G. Xu, X. Gu, Z. Wang, Z. Wang, B. Shi, C. Lu, X. Gong and C. Zhao, *Biomaterials*, 2018, **159**, 82-90.
35. Z. Du, B. Song, W. Zhang, C. Duan, Y. L. Wang, C. Liu, R. Zhang and J. Yuan, *Angew. Chem. Int. Ed.*, 2018, **57**, 3999-4004.
36. R. Wu, Z. Chen, H. Huo, L. Chen, L. Su, X. Zhang, Y. Wu, Z. Yao, S. Xiao, W. Du and J. Song, *Anal. Chem.* , 2022, **94**, 10797-10804.
37. Y. Zhao, Y. Yang, L. Cui, F. Zheng and Q. Song, *Biosens. Bioelectron.*, 2018, **117**, 53-59.
38. Y.-Y. Zhang, H. Zhou, P. Wu, H.-R. Zhang, J.-J. Xu and H.-Y. Chen, *Anal. Chem.*, 2014, **86**, 8657-8664.